IJMMM International Journal of Minerals, Metallurgy and Materials 矿物冶金与材料学报（英文版）

Kinetics of solid-state reduction of chromite overburden

Saida Shaik, Zhiyuan Chen, Preeti Prakash Sahoo, and Chenna Rao Borra

Cite this article as:
Saida Shaik, Zhiyuan Chen, Preeti Prakash Sahoo, and Chenna Rao Borra, Kinetics of solid-state reduction of chromite overburden, *Int. J. Miner. Metall. Mater.*, 30(2023), No. 12, pp. 2347-2355. https://doi.org/10.1007/s12613-023-2681-y

View the article online at SpringerLink or IJMMM Webpage.

International Journal of Minerals, Metallurgy and Materials
Volume 30, Number 12, December 2023, Page 2347
https://doi.org/10.1007/s12613-023-2681-y

Kinetics of solid-state reduction of chromite overburden

Saida Shaik[1)], *Zhiyuan Chen*[2)], *Preeti Prakash Sahoo*[3)], *and Chenna Rao Borra*[1),✉]

1) Metallurgical and Materials Engineering Department, Indian Institute of Technology Kharagpur, Kharagpur, West Bengal 721302, India
2) VITO–Flemish Institute for Technological Research, Boeretang 200, B-2400 Mol, Belgium
3) Research and Development Division, Tata Steel Ltd., Jamshedpur 831001, India
(Received: 23 December 2022; revised: 11 May 2023; accepted: 17 May 2023)

Abstract: The demand for alternative low-grade iron ores is on the rise due to the rapid depletion of high-grade natural iron ore resources and the increased need for steel usage in daily life. However, the use of low-grade iron ores is a constant clinical task for industry metallurgists. Direct smelting of low-grade ores consumes a substantial amount of energy due to the large volume of slag generated. This condition can be avoided by direct reduction followed by magnetic separation (to separate the high amount of gangue or refractory and metal parts) and smelting. Chromite overburden (COB) is a mine waste generated in chromite ore processing, and it mainly consists of iron, chromium, and nickel (<1wt%). In the present work, the isothermal and non-isothermal kinetics of the solid-state reduction of self-reduced pellets prepared using low-grade iron ore (COB) were thoroughly investigated via thermal analysis. The results showed that the reduction of pellets followed a first-order autocatalytic reaction control mechanism in the temperature range of 900–1100°C. The autocatalytic nature of the reduction reaction was due to the presence of nickel in the COB. The apparent activation energy obtained from the kinetics results showed that the solid-state reactions between COB and carbon were the rate-determining step in iron oxide reduction.

Keywords: chromite overburden; solid-state reduction; kinetics; autocatalytic reaction

1. Introduction

India ranks fourth in global chromite production, above one million tons annually. The Sukinda Valley deposits in Orissa state alone account for 98% of the overall chromite in India. During the mining operations of chromite ore in the Sukinda Valley region, above 7.5 million tons of solid waste, i.e., chromite overburden (COB), is generated. The chromium in these waste deposits naturally oxidizes into highly water-soluble chromium (VI), which contaminates the nearby ecosystem. Chromium (VI) is a mutagenic and carcinogenic substance with harmful effects on living organisms. Hence, the utilization of generated wastes as secondary metallic resources has significance owing to the rapid consumption of natural resources in this modern era [1–2].

Many commercial technologies have been developed for the effective utilization of chromite ore processing residue because of the presence of high content of valuable metals (Cr and Ni) [2–3]. To date, no commercial technique has been exploited for the complete utilization of the COB generated in chromite ore production. Plenty of research articles focused on the extraction of chromium and nickel from COB using pyrometallurgical, hydrometallurgical, and bioleaching techniques [4]. However, all these processes are uneconomical and generate a substantial amount of waste. COB comprises 40wt%–50wt% iron oxides, along with chromium (5wt%–20wt%), nickel (<1wt%), silica, magnesia, aluminum, and other metallic values, which can be used as an alternative for low-grade iron ores [5]. Many pyrometallurgical pretreatment methods have become popular for the beneficiation of low-grade iron ores; these methods include the magnetizing roasting iron-making process, sintering iron-making process, and coal-based direct reduction process [5–7]. Magnetizing roasting processes have the advantages of energy saving and low-grade coal use. Although smelting techniques have superb quality of iron output, they are highly energy intensive due to the melting of gangue (silica, alumina, etc.) and require high-quality coke inputs. Coal-based direct reduction techniques are known for their low energy consumption, ease of operation, and less equipment cost [7]. Liang *et al*. [7] obtained iron powder containing 93.10wt% Fe from low-grade iron ore (31wt% Fe) using solid-state reduction of self-reduced pellets, followed by grinding and magnetic separation. This iron can be an excellent feed for steel production industries that use smelting technology. They also claimed that the proposed process is eco-friendlier and more energy conscious compared with existing processes.

The reduction of low-grade iron ore is influenced by several factors, including the type of reducing agent and experimental conditions (temperature of reduction, ore size, ore-to-reductant ratio, etc.). Gupta *et al*. [8] observed that iron oxide

✉ Corresponding author: Chenna Rao Borra E-mail: chenna.borra@metal.iitkgp.ac.in

phases were preferentially reduced over chromium oxide in the solid-state reduction of lean-grade chromite ore within the temperature range of 1100–1250°C Nasr *et al.* [9] have shown that the addition of nickel oxide to iron oxide enhances the reduction degree and lowers the apparent activation energy in the reduction that uses hydrogen gas. They also observed that the formation of the intermediate nickel ferrite phase was responsible for the catalytic nature of the reduction process. Yu and Paktunc [10] also noted that nickel and iron oxides were preferentially reduced over chromium oxide at temperatures below 1500°C, and chromium was reduced to chromium carbide phases at temperatures >1500°C. Table 1 summarizes the activation energies and kinetic models followed by the reduction of iron oxides to different chromite ores. Although several kinetic studies on the carbothermic reduction of oxides in chromite ores have been reported, only a few focused on the iron oxide reduction of lean-grade chromite ores [5,7–9]. The continuous rise in steel consumption and rapid depletion of smelting-grade iron ores prompted industries to search for new technologies based on low-grade iron feed-stocks. The high iron content of COB makes it an effective alternative source in iron production [5]. As per the authors' knowledge, no research studied the reduction kinetics of iron oxide from COB from the perspective of direct reduced iron (DRI) production using COB. Hence, the present work focused on understanding the kinetic behavior and reduction mechanism of composite COB pellets. This study can be crucial in defining the residence time and temperatures of the COB reduction process for metallic iron generation.

Table 1. Review of rate controlling regimes of reduction of chromite ores

Author	Reduction kinetics of iron oxide in chromite ores		
	Temperature range / °C	Rate controlling model	Activation energy / (kJ.mol^{-1})
Nasr *et al.* (>1wt% NiO) [9]	900–1200	Interfacial chemical reaction	56.5–80.1
Reddy *et al.* [11]	700–1100	Avrami–Erofeev equation; $n = 1$	23–55.8
Chakraborty *et al.* [12]	900–1300	Ginstling–Brounshteion (GB)	135
Sundar Murti and Seshadri [13]	1150–1300	Ginstling–Brounshteion (GB)	130
Gupta *et al.* [8]	1100–1250	Avrami–Erofeev equation; $n = 1$	38.52
Wright *et al.* [14] (Hematite ore + Char coal)	900–1200	Autocatalytic or first-order kinetic equation	290–335

Note: n—order of the reaction.

2. Experimental

2.1. Materials

The COB sample used in this study was collected from the mining disposal waste of chromite ore located in the Sukinda Valley region, India. The moisture content, volatile matter, ash, and fixed carbon content in coal samples were measured in accordance with the American Society for Testing Materials (ASTM) standards: ASTM D3173, ASTM D4239, ASTM D3174, and ASTM D5142 [15–16]. X-ray fluorescence (XRF) analysis was used to analyze the remaining raw materials used in this study (Table 2). This process showed that iron oxides, silica, chromium oxide, alumina, and magnesia were the major oxides in the COB, and the NiO content was less than 1wt%. Hence, the reduction of nickel oxides was neglected in the present study.

Table 2. XRF analysis of the raw materials used in this study wt%

Raw material	Fe_2O_3	Cr_2O_3	NiO	MgO	Al_2O_3	SiO_2	CaO	Fixed carbon	Volatile matter	Ash	LOI
COB	66.71	8.28	0.83	2.8	3.3	10.8	—	—	—	—	7.28
Coal	—	—	—	0.2	2.3	4.21	0.51	71.5	12	9.28	—
Bentonite	1.8	0.1	—	1.44	14.58	65.56	0.9	—	—	—	15.62

Note: LOI—loss of ignition.

2.2. Pelletization procedure and reduction experiments

The as-received COB ore was grounded to <100 μm and dried at 110°C for 12 h. The devolatilized anthracite coal (25.3 g for 100 g COB) with a size of <100 μm was used as the reducing agent. Bentonite clay (1wt%) was used as a binder during the pelletization. All raw materials were weighed accurately and mixed well before charging in the disk pelletizer. The output green pellets were dried in an electric oven at a temperature of 110°C for 12 h.

Before the experimental work, FactSage 6.4 thermodynamic software package was used to plot the free energy change versus the temperature plots of the required chemical reactions. FactPS and FTOxid databases were selected to plot the free energy curves of different chemical reactions. Isothermal and non-isothermal thermo-gravimetric analyses (TGA) of pellets were performed in bulk TGA involving a vertical alumina tube furnace supported with a weighing balance at the top of the tubular furnace (Fig. 1). The sample was hung from the bottom of the balance to the middle of the heating zone of the furnace by a Pt wire. The balance was connected to a computer for data acquisition. Any weight change during the experiment was collected with respect to

time. The furnace was also connected to the computer for data acquisition, and the temperature was obtained with respect to time. Argon gas was purged continuously into the furnace to attain inert conditions. The flow rate of argon gas and the heating rate were maintained at 200 mL/min and 2.5°C/min, respectively. The furnace temperature was controlled using a programmable electric controller with an efficiency of ±1°C. Non-isothermal experiments were conducted to determine the phase changes or reduction temperature zone in the COB composite pellets. For the non-isothermal study, all the raw materials (COB, coal, and bentonite) were dried before pelletization. After the search for the reduction zone, isothermal experiments were performed to investigate the optimum time and temperature for the maximum reduction of the COB composite pellets. For the isothermal kinetics study, the calcined COB (at a temperature of 200°C), devolatilized coal, and bentonite (at a temperature of 900°C) were used to prepare the COB composite pellets to determine the real weight loss caused by the reduction process. The amount of coal (equivalent carbon present in the coal and based on 100vol% CO formation at 900°C) required for the complete reduction of iron oxide and nickel oxide in the COB was used to prepare self-reducing pellets.

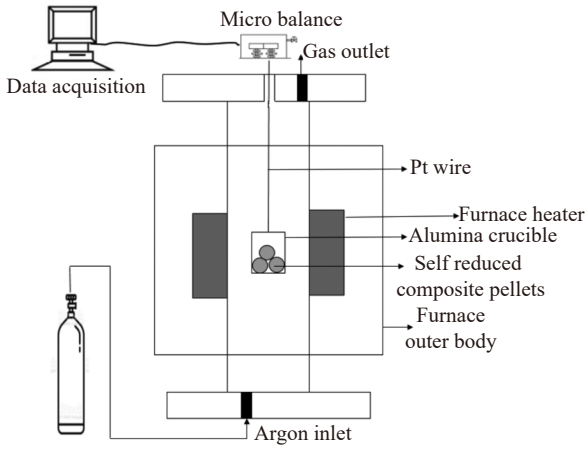

Fig. 1. Tubular furnace setup used in the reduction of COB pellets.

2.3. Characterization techniques

X-ray diffraction (XRD) analysis was conducted using a Philips X-ray diffractometer with Cu K_α radiation (k = 1.5406 Å), an operating voltage of 40 kV, and a constant current of 40 mA during the analysis. A JEOL JXA-6400 scanning electron microscope attached to a KEVEX super-dry energy-dispersive X-ray detector was used for the visual identification of phases and elemental analysis of reduced pellet samples.

3. Results and discussion

3.1. Characterization of ore

Table 2 shows the XRF analysis results of the COB sample and other raw materials. The COB contained high contents of iron oxide and silica (~10wt%) as the major components, along with low amounts of chromium (~8wt%), alumina, magnesia, and nickel. Fig. 2 displays the XRD pattern of the new COB. The results showed that the COB material used in the present study was mainly composed of goethite, silica, chromite, and other gangue mineral phases, and the chromite present in the ore existed in spinel form (C–(Fe,Mg)(Cr,Fe,Al)$_2$O$_4$). Bhaskar and Bhoi [17] also observed that after the processing of COB, most of the iron existed in goethite form along with silica and chromite.

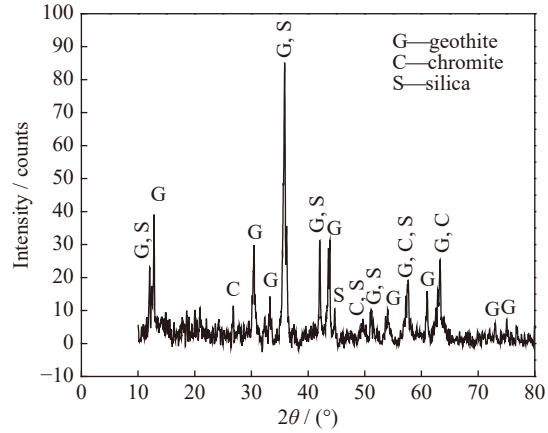

Fig. 2. X-ray diffraction pattern of chromite overburden.

3.2. Thermodynamic analysis

Fig. 3 indicates the free energy associated with the formation of different oxide compounds in the COB ore obtained using FactSage software [18]. The plot of the minimum reduction temperature of oxide is the point at which CO and CO_2 formation lines cross over the respective oxide free energy on the formation line. The equilibrium plots show that the conversions of hematite to magnetite, magnetite to wustite, and wustite to metallic iron were feasible at temperatures above 350, 650, and 800°C, respectively. Nickel oxide was the first compound to be reduced to metallic form at twice the low temperature (400°C) of iron oxide reduction

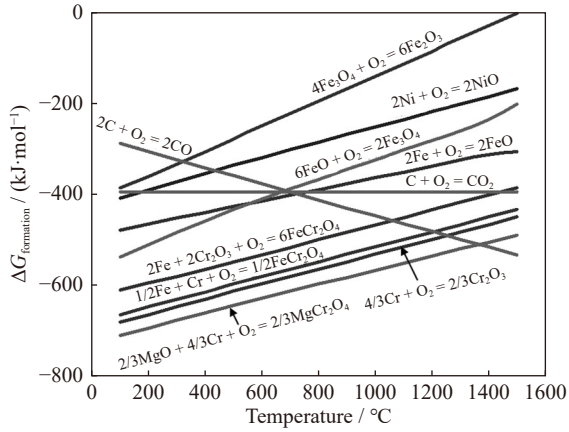

Fig. 3. Free energy of the formation of compounds ($\Delta G_{formation}$) in the chromite overburden ore and coal gasification at different temperatures.

[9,19]. The diagram also reveals that at temperatures below 750°C, CO_2 was the gas product obtained in the reduction process, and beyond 750°C, the produced gas was mostly composed of CO. Hence, the reactions involved in nickel formation and conversion of hematite to magnetite and magnetite to wustite produced CO_2 gas during carbon reduction. The magnesium chromite spinel solution had a higher negative free energy compared with the iron chromite spinel and free chromite structures. Hence, all chromium oxides in the COB ore existed in magnesium chromite form, which has a high reduction temperature (1400°C). Eqs. (1)–(6) show the major reactions that occurred in the solid-state reduction of COB ore.

$$3Fe_2O_3(s)+C(s)=2Fe_3O_4(s)+CO(g), T>800°C \quad (1)$$

$$3Fe_2O_3(s)+CO(g)=2Fe_3O_4(s)+CO_2(g), T<800°C \quad (2)$$

$$Fe_3O_4(s)+CO(g)=3FeO(s)+CO_2(g) \quad (3)$$

$$FeO(s)+CO(g)=Fe(s)+CO_2(g) \quad (4)$$

$$C(s)+CO_2(g)=2CO(g), T>800°C \quad (5)$$

$$2NiO(s)+C(s)=2Ni(s)+CO_2(g) \quad (6)$$

$$FeCr_2O_4(s)+C(s)=Fe(s)+Cr_2O_3(s)+CO(s) \quad (7)$$

$$MgO(s)+Cr_2O_3(s)=MgCr_2O_4(s) \quad (8)$$

where (s)—solid, (g)—gas, and T represents temperature.

In reality, the equilibrium temperatures of reduction reactions may be higher due to the slow kinetics or lower due to the formation of carbides or solid solutions. The reaction in Eq. (5), which is the solution loss reaction, occurs due to the formation of CO_2 gas at high temperatures (T > 800°C).

3.3. Thermo-gravimetric analysis

Non-isothermal reduction experiments of pellets were undertaken to investigate the phase changes in the reduction process at various temperatures through TGA. The results were compared with those of raw COB powder for comparison. Fig. 4 shows the TGA graph of the COB powder and pellets, where the percentage of weight change is given with respect to temperature. The TGA curves show that the COB powder lost about 7% of its mass at temperatures up to 355°C (point *D*), and beyond this temperature, the mass loss became stagnant. These losses were attributed to the presence

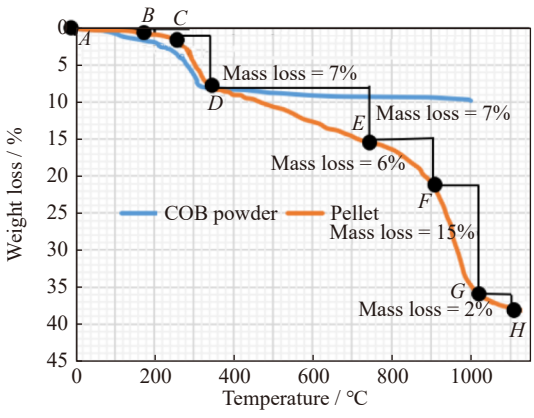

Fig. 4. TGA of COB powders and pellets.

of moisture content (*A*–*B* regions) and the decomposition of hydrate molecules associated with goethite and other compounds (*B*–*C* and *C*–*D* regions). Weissenborn *et al*. [20] also observed a similar "z" curve in the TGA analysis of a standard goethite sample; they stated that the decomposition of goethite occurred in the temperature range of 250–355°C. For the XRF analysis of chromite ore and with the application of Eq. (9), ~7.5% mass loss was calculated to be due to goethite decomposition (with consideration that the 100wt% iron oxide is goethite). This value is higher than the experimental TGA value, which confirmed the association of some iron with the chromite spinel phase observed in the XRD results (Fig. 2).

$$2FeOOH(s)=Fe_2O_3(s)+H_2O(g) \quad (9)$$

The composite pellet sample exhibited mass loss (~38%) at temperatures up to 1100°C. The pellet sample showed a negligible change in the *A*–*B* region because of the drying of pellets prior to the experiments. The calculated mass loss in the curve of the pellet sample until region *C*–*D* was 7%, which accounted for goethite decomposition as discussed earlier. After point *D*, the mass loss in TGA was contributed to the loss of volatile matter and coal gasification due to the reaction with oxygen in NiO and iron oxide. The mass loss (~7%) in the *D* to *E* region was attributed to the release of volatile matter (~3% mass loss from 25.3 g coal in pellets) and gasification due to hematite to magnetite reduction (~3.13% mass loss according to Eq. (1)) [21]. The nickel oxide present in the ore also reduced in the temperature range of the *D* to *E* region [5] and contributed ~0.3% mass loss according to stoichiometric calculations obtained using Eq. (6). Kapure *et al*. [5] also stated that nickel metal formation enhances the reduction of iron oxide by increasing the tendency of CO formation through the Boudouard reaction (Eq. (5)). The mass loss in the *E* to *F* region was due to magnetite to wustite conversion, which accounted for 6% mass loss in the curve; however, the value reached 6.3% in the stoichiometric condition. The reduction of wustite to metallic iron contributed 15% mass loss in the *F* to *G* region [22]. In the *G* to *H* region, the 2% mass loss was due to the reduction of iron associated with the chromite spinel phase [5].

3.4. Isothermal reduction of COB pellets

Isothermal experiments were conducted at five different temperature intervals between 900 to 1100°C for 60 min, and the obtained data are displayed in Fig. 5. The fraction of iron formed was calculated through subtraction of the losses due to moisture, goethite decomposition, and volatile matter content from the original weight loss obtained from the weighing balance. The fraction of iron formation increased with time and temperature. The conversion rate was high at temperatures above 1000°C, the maximum reduction was obtained at temperatures above 1100°C within 15 min time intervals, and the reduction curve was saturated after this point. The rapid conversion of iron at temperatures above 1000°C may be due to the high gasification tendency of coal at these

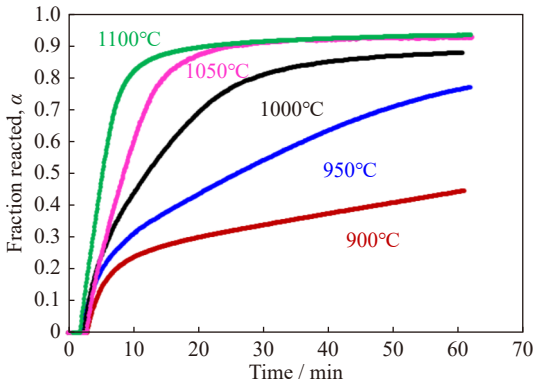

Fig. 5. Effect of time and temperature on the reaction fraction in the pellets.

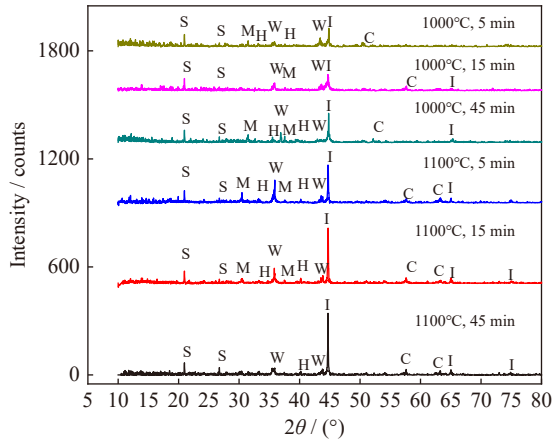

Fig. 6. XRD analysis of reduced pellets (C: chromite; S: SiO_2; M: Fe_3O_4; H: Fe_2O_3; I: metallic iron; W: wustite).

temperatures [22–23].

3.5. Analysis of evolution of mineral phases in self-reduced pellets

The mineralogical changes that occurred during the reduction of COB ore at different temperatures and time intervals were investigated by furnace cooling of reduced pellet samples followed by XRD analysis (Fig. 6). The results showed that the intensity of iron oxide diffraction peaks decreased sharply with an increase in reduction time at 1000°C and 1100°C. After 5 min of reduction at 1000°C, the wustite, hematite, and magnetite diffraction peak intensities enlarged and weakened as the reduction time increased to 15 and 45 min. Silica and chromite phase peaks were also detected in XRD analysis. However, no change was observed in the intensities of silica and chromite phases as the reduction time increased, which indicates the selective reduction of iron oxides in the self-reduced pellets. At 1000°C, most of the magnetite and hematite phases were reduced to wustite but showed less effect on wustite reduction. However, with the rise in temperature to 1100°C, the wustite phase peaks disappeared gradually over time. Fig. 7 shows the microstructural evolution of COB pellets with time at 1100°C. At the initial time (5 min), large gray particles and a smaller number of bright particles were observed. As the time was extended to 45 min (Fig.7(d)), the number of bright particles increased. Fig. 7(e) and (f) and Table 3 represent the energy-dispersive spectroscopy (EDS) analysis of gray and bright particles. The gray particles represent the unreduced COB that contained high amounts of Fe, Cr, and Si, along with oxygen. The bright particles included reduced Fe along with minor quantities of Cr and Ni metals. An oxygen peak was observed in the bright particles, which indicates the loss of oxygen due to the reduction of COB. In addition, bright metallic iron phases were liberated well from chromite and the gangue minerals. Hence, iron can be separated from COB by magnetic separation or other gravity separation processes [7].

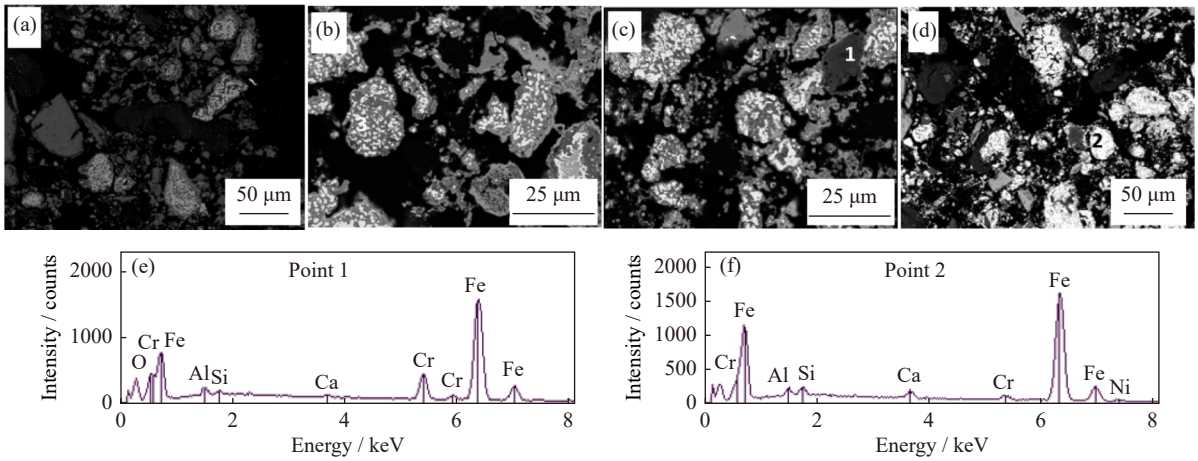

Fig. 7. Scanning electron microscopy image of a partially reduced COB sample at 1100°C at different reduction times: (a) 5, (b) 15, (c) 30, and (d) 45 min. EDS analyses of points 1 (e) and 2 (f).

Table 3. EDS analysis of the points shown in Fig. 7 wt%

Point	O	Na	Mg	Al	Si	K	Ca	Cr	Mn	Fe	Ni	Mo
Point 1	32.0	1.55	0.58	14.2	12.8	0.43	9.05	9.73	0.98	18.0	—	0.67
Point 2	—	—	—	—	—	—	—	2.02	—	96.4	1.58	—

4. Kinetics of COB pellet reduction

A number of solid–gas reaction models have been developed, and some of them have been applied to the solid-state reduction of ore. Two mathematical model methods have been developed to define reduction kinetics: (i) integral and (ii) differential methods. The integral method assumes that the entire reduction process follows a single kinetic model equation [21–24]; the integral kinetic model used equations to determine the kinetics of COB reduction in the present study (Table 4).

To determine the appropriate model equation, we fitted the experimental data of a fraction of reduction with a variation in integral equations by keeping the fraction of reduction on the *Y*-axis and time on the *X*-axis. The equation with a high correlation coefficient was considered the kinetic model governing equation of the reduction process. The rate constant data obtained from the appropriate curve fitting were used for the activation energy and frequency factor calculations of pellet reduction using the Arrhenius equation [21] (Eq. (15)). In contrast to the above procedures, the differential method disregards any kinetic model equation to calibrate experimental data. In this method, the time required for a constant fraction of conversion is estimated at different temperatures. Plots are constructed using $\ln t_\alpha$ on the *Y*-axis and $1/T$ on the *X*-axis, and the activation energy is calculated from the slopes obtained from fitting. The generalized differential method equation is given in Eq. (16), from which the activation energy is calculated for a particular reaction process irrespective of the rate-determining step [25–26].

Table 4. Kinetic model equations derived using integral methods

Type of kinetic equation	Model equation	Eq.
Nucleation first-order reaction	$-\ln(1-\alpha) = kt$	(10)
The chemical reaction model equation (Sphere)	$1-(1-\alpha)^{1/3} = kt$	(11)
Diffusion: Jander equation	$\left(1-(1-\alpha)^{1/3}\right)^2 = kt$	(12)
Diffusion: Ginstling–Brounshteion (GB)	$1-2\alpha/3-(1-\alpha)^{2/3} = kt$	(13)
Diffusion: Zhuravlev–Lesokhin–Tempelman (ZLT)	$\left((1-\alpha)^{-1/3}-1\right)^2 = kt$	(14)

$$\ln k = \ln A - \frac{E_a}{RT} \tag{15}$$

where k is the rate constant, A represents the frequency factor, R refers to the universal gas constant, T is the temperature, and E_a indicates the apparent activation energy.

$$\ln t_\alpha = \ln[A \cdot g(\alpha)] + \frac{E_d}{RT} \tag{16}$$

where α represents the fraction of conversion, E_d is the activation energy, t_α denotes the reaction time required to attain a particular α at infinite temperature, and $g(\alpha)$ refers to the possible integral kinetic model.

Fig. 8 presents the fitting of experimental model data in the integral kinetic model equations given in Table 4 for COB pellet reduction at 900 and 1050°C. The experimental data fit well the autocatalytic kinetic model equation with a high correlation coefficient (R^2 = 0.9994 and 0.9966 at 900 and 1050°C, respectively) compared with other kinetic models. This finding was also observed under other reduction temperatures from 900 to 1100°C. Fig. 9 displays the fitting of experimental data values in the autocatalytic model equation at five different temperatures. Table 5 shows the rate constants obtained from the autocatalytic equation. The rate constants increased continuously with the temperature, but a sudden jump in their values was observed with the increase in the temperature from 1000 to 1050 and 1100°C. This condition resulted in the high amount of metallic iron phase obtained in the XRD analysis (Fig. 6) of the samples reduced at 1100°C for 15 min compared with those reduced at 1000°C. This sudden rise in the rate constant may be attributed to the high coal gasification (CO formation) at high temperatures, which aided in iron oxide reduction [22]. In real scenarios, the kinetics model equations do not pass through the origin,

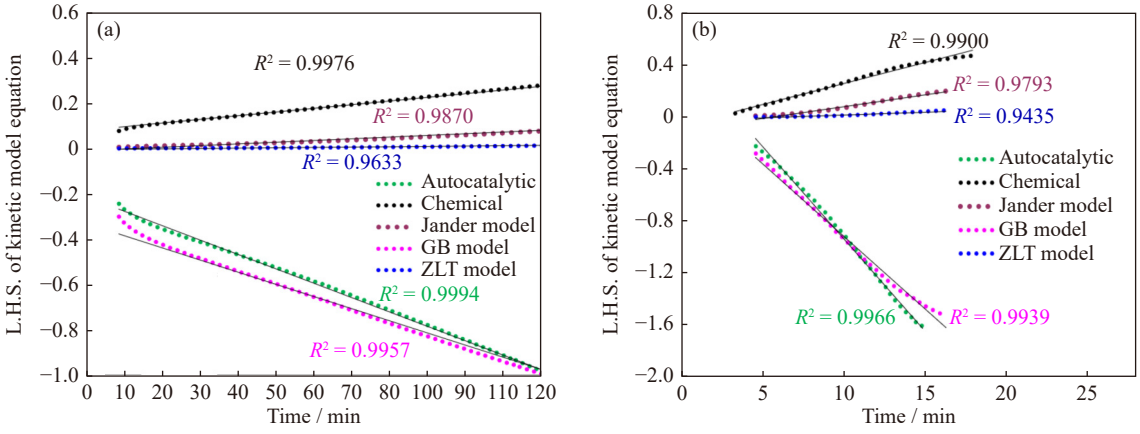

Fig. 8. Plots of the left-hand side (L.H.S.) of Eqs. (10)–(14) versus time of reduction at (a) 900°C and (b) 1050°C.

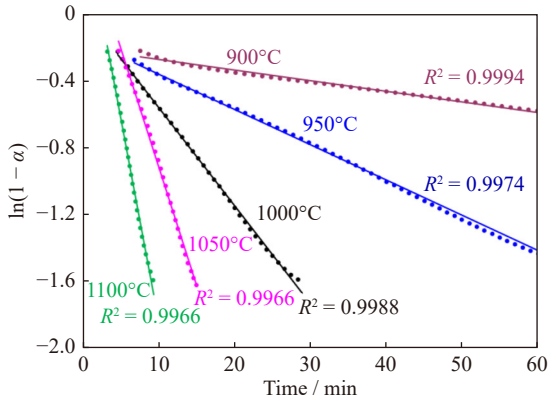

Fig. 9. Negative rate constant (k, min^{-1}) values obtained at five different temperatures using the autocatalytic reaction equation (thick lines represent the fitting curve equation).

which can be attributed to the additional reaction steps in short periods that are generally excluded. For example, residue goethite decomposition, carbon monoxide build-up, or carbon gasification causes a positive intercept [20–24]. Fig. 10 shows the negative natural logarithm of rate constants versus the inverse of the temperature plot, which was used to determine the activation energy and frequency factor values using Eq. (15). Table 5 presents the values obtained from the plot, which shows that the calculated apparent activation energy and frequency constant for COB reduction were 237 kJ/mol and 2.7 × 10^7, respectively. Fig. 11 displays the plots of calculated activation energy obtained via the differential method, in which the inverse of temperature was on the X-axis, and $\ln t_\alpha$ was on the Y-axis. Table 6 provides the activation energy values obtained from the plot, it shows that the activation energy varied between 70.68 to 290.66 kJ/mol under the given temperature range. The variation in activation energy indicates the stepwise reduction mechanism of iron oxide in the presence of reducing agents, which has been described by Wei *et al.* [23] and Chen *et al.* [25].

Table 5. Kinetic parameters obtained from the autocatalytic rate equations at different temperatures

Temperature / °C	Rate constant / (min^{-1})	Activation energy / (kJ·mol^{-1})	Frequency factor
900	0.006		
950	0.021		
1000	0.058	237	2.7 × 10^7
1050	0.142		
1100	0.241		

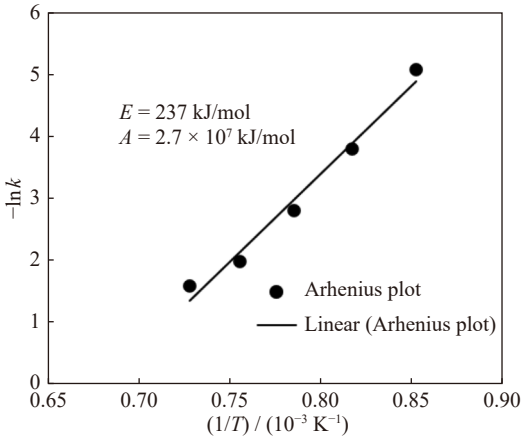

Fig. 10. $\ln k$ versus $-1/T$ plots of the rate constants obtained from the autocatalytic model equation.

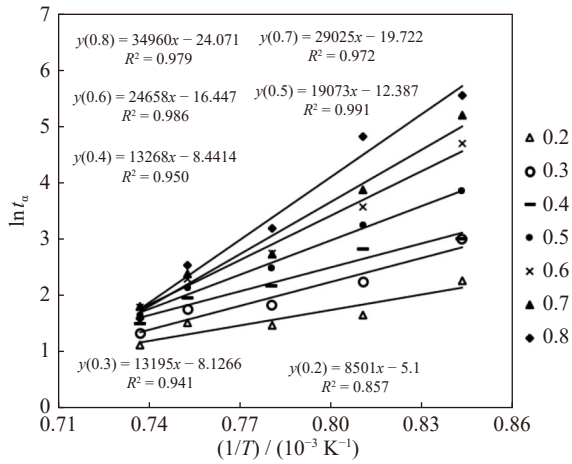

Fig. 11. $\ln t_\alpha$ versus $1/T$ plot of the calculated activation energy obtained using the differential methods (Eq. (16)).

Table 6. Activation energy values calculated using Fig. 11 and Eq. (16)

Fraction (α)	E_d / (kJ·mol^{-1})
0.2	70.68
0.3	109.70
0.4	110.31
0.5	158.57
0.6	205.01
0.7	241.31
0.8	290.66

Thermodynamic parameters, such as the change in activation enthalpy (ΔH^*) and activation entropy change (ΔS^*), were calculated using the Eyring equation (Eq. (17)). From the enthalpy and entropy values, the change in the activation Gibbs free energy (ΔG^*) was calculated according to Eq. (18) [26].

$$\ln\frac{k}{T} = -\frac{\Delta H^*}{RT} + \ln\frac{k_B}{h} + \frac{\Delta S^*}{R} \quad (17)$$

$$\Delta G^* = \Delta H^* - T\Delta S^* \quad (18)$$

where k_B is the Boltzmann constant, and h is Planck's constant. Fig. 12 shows the thermodynamic Eyring plot, which exhibits a straight line with the slope and intercepts equal to $\frac{-\Delta H^*}{R}$ and $\ln\frac{k_B}{h} + \frac{\Delta S^*}{R}$. From the plots, the changes in ΔH^* and ΔS^* were calculated as 223.67 kJ·mol^{-1} and −104.12 J·K^{-1}·mol^{-1}, respectively. A positive ΔH^* value represents an endothermic characteristic of the reduction process, and a negative ΔS^* value indicates an ordered structure in the product phase [27]. Table 7 indicates the kinetic and thermodynamic parameters of the carbothermic reduction of COB. The ΔG^* values for the reduction process were positive and

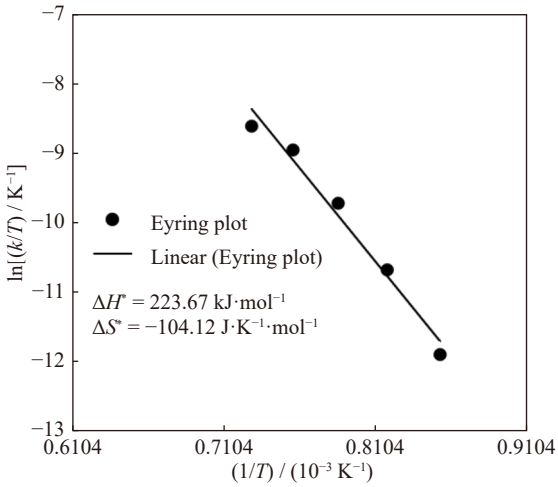

Fig. 12. Plot of ln[(k/T) / K^{-1}] versus the reciprocal of temperature.

increased with the temperature rise. The positive apparent free energy indicates that the COB reduction process was not spontaneous, and an external driving force must be supplied to the system to initiate product formation. From the positive ΔH^* and negative ΔS^* results, the apparent reduction reaction of iron oxides in chromite ore is akin to the direct reduction reaction [28–30]:

$$FeO_x + C = FeO_{x-1} + CO \quad (19)$$

Table 7. Kinetic and thermodynamic parameters of the COB reduction process

T / °C	ΔG^* / (kJ·mol^{-1})	A	E / (kJ·mol^{-1})	ΔH^* / (kJ·mol^{-1})	ΔS^* / (J·K^{-1}·mol^{-1})
900	345.80				
950	351.01				
1000	356.21	2.7×10^7	237	223.67	−104.12
1050	361.42				
1100	366.63				

5. Conclusions

The following conclusions were drawn from this work.

(1) Goethite, silica, and chromite were the major mineral phases detected in the COB sample. Bulk chemical analysis showed that alumina, magnesia, and nickel were also present as minor components in the COB sample.

(2) In the solid-state reaction of COB pellets, only iron oxide and nickel oxide reduction occurred under experimental conditions. Meanwhile, silica, chromite, and alumina remained in oxide forms under reduction conditions. The solid-state reduction of iron oxides in the COB pellets followed the autocatalytic reaction model; the calculated apparent activation energy and frequency factor were 237 kJ·mol^{-1} and 2.7×10^7, respectively. Kinetic equations of the differential method showed that the activation energies during COB reduction varied between 70.68 to 290.66 kJ·mol^{-1} at the temperature range of 900–1100°C.

(3) The changes in ΔH^* and ΔS^* in the COB reduction process were calculated using the Eyring equation, with results of 223.67 kJ·mol^{-1} and −104.12 J·mol^{-1}·K^{-1}, respectively. Positive ΔH^* and negative ΔS^* changes indicate that COB reduction was dominated mostly by solid-state reduction reactions.

(4) This work may help in the application of lean-grade iron ore as feed for steel industries through subsequent grinding and magnetic separation to produce high-grade metallic iron powder.

Conflict of Interest

All authors confirm that they have no competing interests or financial ties that could influence the outcomes or interpretation of this research.

References

[1] S. Biswas, S. Samanta, R. Dey, S. Mukherjee, and P.C. Banerjee, Microbial leaching of chromite overburden from sukinda mines, Orissa, India using *Aspergillus niger*, *Int. J. Miner. Metall. Mater.*, 20(2013), No. 8, p. 705.

[2] X.R. Zhang, G. Li, J. Wu, N. Xiong, and X.J. Quan, Leaching of valuable elements from the waste chromite ore processing residue: A kinetic analysis, *ACS Omega*, 5(2020), No. 31, p. 19633.

[3] T.G. Wang, M.L. He, and Q. Pan, A new method for the treatment of chromite ore processing residues, *J. Hazard. Mater.*, 149(2007), No. 2, p. 440.

[4] S.K. Behera, S.K. Panda, N. Pradhan, L.B. Sukla, and B.K. Mishra, Extraction of nickel by microbial reduction of lateritic chromite overburden of Sukinda, India, *Bioresour. Technol.*, 125(2012), p. 17.

[5] G.U. Kapure, C.B. Rao, V.D. Tathavadkar, and R. Sen, Direct reduction of low grade chromite overburden for recovery of metals, *Ironmaking Steelmaking*, 38(2011), No. 8, p. 590.

[6] Y. Cao, Y.S. Sun, P. Gao, Y.X. Han, and Y.J. Li, Mechanism for suspension magnetization roasting of iron ore using straw-type biomass reductant, *Int. J. Min. Sci. Technol.*, 31(2021), No. 6, p. 1075.

[7] Z.K. Liang, L.Y. Yi, Z.C. Huang, B.Y. Huang, and H.T. Han, A novel and green metallurgical technique of highly efficient iron recovery from refractory low-grade iron ores, *ACS Sustainable Chem. Eng.*, 7(2019), No. 22, p. 18726.

[8] P. Gupta, A.K. Bhandary, M.G. Chaudhuri, S. Mukherjee, and R. Dey, Kinetic studies on the reduction of iron oxides in low-grade chromite ore by coke fines for its beneficiation, *Arab. J. Sci. Eng.*, 43(2018), No. 11, p. 6143.

[9] M.I. Nasr, A.A. Omar, M.H. Khedr, and A.A. El-Geassy, Effect of nickel oxide doping on the kinetics and mechanism of iron oxide reduction, *ISIJ Int.*, 35(1995), No. 9, p. 1043.

[10] D.W. Yu and D. Paktunc, Kinetics and mechanisms of the carbothermic reduction of chromite in the presence of nickel, *J. Therm. Anal. Calorim.*, 132(2018), No. 1, p. 143.

[11] R. G. Reddy, R. B. Inturi, and M. V. Klein, Low temperature reduction of chromite ores with carbon, [in] *EPD Congress Proceedings Sessions and Symposium*, Warrendale, 1998, p. 697.

[12] D. Chakraborty, S. Ranganathan, and S.N. Sinha, Investigations on the carbothermic reduction of chromite ores, *Metall. Mater. Trans. B*, 36(2005), No. 4, p. 437.

[13] N.S. Sundar Murti and V. Seshadri, Kinetics of reduction of synthetic chromite with carbon, *ISIJ Int.*, 22(1982), No. 12, p.

925.
[14] J.K. Wright, K.M. Bowling, and A.L. Morrison, Reduction of hematite pellets with carbonized coal in a static bed, *ISIJ Int.*, 21(1981), No. 3, p. 149.
[15] S. Saida, S. Chakravaty, R.N. Sahu, R. Biswas, and K. Chakravarty, Laboratory-scale tests for the utilization of high ash non-coking coal in coke-making process, *Trans. Indian Inst. Met.*, 73(2020), No. 5, p. 1257.
[16] S. Shaik, S. Chakravarty, P.R. Mishra, R.N. Sahu, and K. Chakravarty, Caking ability tests for coal blends in process to utilize the Indian origin coals, *Trans. Indian Inst. Met.*, 72(2019), No. 12, p. 3129.
[17] K.L. Bhaskar and B. Bhoi, Iron and nickel enrichment in low grade chromite overburden to produce ferronickel alloys, *Trans. Indian Inst. Met.*, 74(2021), No. 6, p. 1321.
[18] C.W. Bale, P. Chartrand, S.A. Degterov, *et al*., FactSage thermochemical software and databases, *Calphad*, 26(2002), No. 2, p. 189.
[19] X.M. Lv, W. Lv, Z.X. You, X.W. Lv, and C.G. Bai, Non-isothermal kinetics study on carbothermic reduction of nickel laterite ore, *Powder Technol.*, 340(2018), p. 495.
[20] P.K. Weissenborn, J.G. Dunn, and L.J. Warren, Quantitative thermogravimetric analysis of haematite, goethite and kaolinite in Western Australian iron ores, *Thermochim. Acta*, 239(1994), p. 147.
[21] E. Donskoi, D.L.S. McElwain, and L.J. Wibberley, Estimation and modeling of parameters for direct reduction in iron ore/coal composites: Part II. Kinetic parameters, *Metall. Mater. Trans. B*, 34(2003), No. 2, p. 255.
[22] Y. Man, J.X. Feng, Y.M. Chen, and J.Z. Zhou, Mass loss and direct reduction characteristics of iron ore-coal composite pellets, *J. Iron Steel Res. Int.*, 21(2014), No. 12, p. 1090.
[23] R.F. Wei, D.Q. Cang, L.L. Zhang, and Y.Y. Bai, Staged reaction kinetics and characteristics of iron oxide direct reduction by carbon, *Int. J. Miner. Metall. Mater.*, 22(2015), No. 10, p. 1025.
[24] J.L. Zhang, Y. Li, Z.J. Liu, *et al*., Isothermal kinetic analysis on reduction of solid/liquid wustite by hydrogen, *Int. J. Miner. Metall. Mater.*, 29(2022), No. 10, p. 1830.
[25] Z.Y. Chen, C. Zeilstra, J. Van Der Stel, J. Sietsma, and Y.X. Yang, Thermal decomposition reaction kinetics of hematite ore, *ISIJ Int.*, 60(2020), No. 1, p. 65.
[26] S. Ali, Y. Iqbal, I. Khan, *et al*., Hydrometallurgical leaching and kinetic modeling of low-grade manganese ore with banana peel in sulfuric acid, *Int. J. Miner. Metall. Mater.*, 28(2021), No. 2, p. 193.
[27] N. Birkner and A. Navrotsky, Thermodynamics of manganese oxides: Effects of particle size and hydration on oxidation-reduction equilibria among hausmannite, bixbyite, and pyrolusite, *Am. Mineral.*, 97(2012), No. 8-9, p. 1291.
[28] P. Gao, G.F. Li, X.T. Gu, and Y.X. Han, Reduction kinetics and microscopic properties transformation of boron-bearing iron concentrate–carbon-mixed pellets, *Miner. Process. Extr. Metall. Rev.*, 41(2020), No. 3, p. 162.
[29] M. Kumar and S.K. Patel, Assessment of reduction behavior of hematite iron ore pellets in coal fines for application in sponge ironmaking, *Miner. Process. Extr. Metall. Rev.*, 30(2009), No. 3, p. 240.
[30] H.U. Ross, The fundamental aspects of iron ore reduction, [in] *Symposium on Science and Technology of Sponge Iron and its Conversion to Steel*, Jamshedpur, 1973, p. 134.